Peer-reviewed version available at *Int. J. Mol. Sci.* **2020**, *21*, 6714; doi:10.3390/ijms21186714

Doubly-charged negative ions as novel tunable catalysts: graphene and fullerene molecules versus atomic metals

Kelvin Suggs and Alfred Z. Msezane
Clark Atlanta University, Department of Physics and CTSPS, Atlanta, Georgia 30314, USA

Abstract

The fundamental mechanism underlying negative-ion catalysis involves bond-strength breaking in the transition state (TS). Doubly-charged atomic/molecular anions are proposed as novel dynamic tunable catalysts and demonstrated in water oxidation to peroxide. Density Functional Theory TS calculations have found tunable energy activation barrier reduction ranging from 0.030 eV to 2.070eV, with Si^{2-}, Pu^{2-}, Pa^{2-} and Sn^{2-} the best catalysts; the radioactive elements usher in new application opportunities. C_{60}^{2-} reduces significantly the standard C_{60}^{-} TS energy barrier while graphene increases it, behaving like cationic systems. Rank-ordered catalysts according to their reaction barrier reduction efficiency, variation across charge states and systems reveal their tunable and wide applications, ranging from water purification to biocompatible anti-viral and anti-bacterial sanitation systems.

Keywords: Graphene, fullerenes, atomic metals, doubly-charged anions, tunable catalysts, electron scattering, water oxidation

1. Introduction

The importance of the need to understand the fundamental functional roles of the various constituents of current complicated catalysts is demonstrated in the recent investigation of the water oxidation catalyzed by the oxygen-evolving complex of photosystem II [1]. Also pursued by these authors is the development of new artificial water oxidation catalysts for artificial photosynthetic water oxidation [2]. In recent years research on water oxidation catalyzed by various systems, processes and mechanisms has intensified [3-16]. The advent of the COVID-19 pandemic has also accelerated the vigorous search for and synthesis of atomic nanoparticles and catalysts for various applications, see for examples [17, 18]. Of particular interest here is also the stability of organic solar cells required before their actual commercialization [19]. The use of fullerenes with large electron affinities (EAs) is part of the recommended solution [19]. The formation of the high energy singlet oxygen and the super oxygen radical anions, contributing to the degradation mechanism of the employed polymers, could be mitigated through the use of appropriate tunable catalysts presented in this paper.

Here we propose using doubly-charged atomic/molecular negative ions as novel tunable catalysts for general applications. Their effectiveness is demonstrated in catalyzing the water oxidation to peroxide process. The fundamental mechanism underlying negative-ion catalysis involves anionic molecular complex formation in the transition state (TS), with the atomic/molecular negative ion breaking up the hydrogen bond strength. The oxidation reaction to be catalyzed, considered here is $2H_2O + O_2 \rightarrow 2H_2O_2$ as opposed to that discussed in [1] $2H_2O \rightarrow H_2O_2 + H_2$. The strict procedure followed here is to first bring the anionic catalyst, say Au^- to the water to break up the hydrogen-bond strength and then follow with the addition of O_2 to form the desired H_2O_2. This process can be contrasted with the well investigated muon (μ) catalyzed nuclear fusion cycle wherein is involved the resonant formation of the muonic molecular ion, $dt\mu$ [20], with *d* and *t* being the deuteron and the triton, respectively. Consequently, this paper investigates the energy barrier reduction during the water oxidation catalyzed by various doubly-charged negative atomic/molecular ions with Z varying from 14 through the lanthanide atoms to the interesting radioactive actinides. Also included is the purely radioactive element 85, At whose EA has been measured in a recent

breakthrough experiment [21]. Astatine is the heaviest naturally occurring halogen and its isotope ^{211}At is remarkably well suited for targeted radionuclide therapy for cancer. Data for the doubly-charged fullerenes C_{60}^{2-}, C_{20}^{2-} and C_{136}^{2-} as well as those of Gr^{2-} are also contrasted with those of their singly-charged counter parts. The results demonstrate the dynamic catalytic behavior of the atomic/molecular systems.

The Royal Society of Chemistry published the themed collection "Single Atoms as Catalysts" [22] to celebrate the International Year of the Periodic Table. Naturally, this has been followed by the investigation of single fullerene negative ions as catalysts [23]. Their effectiveness has been demonstrated in catalyzing the processes of the oxidation of water to peroxide and water synthesis from H_2 and O_2 using the fullerene anions from C_{44}^- to C_{136}^-. Density Functional Theory (DFT) calculations found the C_{60}^- anion to be optimal; namely, reduce the TS energy barrier by the same amount in the oxidation of water to peroxide and water synthesis from H_2 and O_2. Importantly, DFT also found the C_{136}^- anion to represent the best catalyst for both water oxidation to peroxide and water synthesis from H_2 and O_2. Indeed, it has been found that the catalytic effectiveness, decreasing the energy barrier, increased with the fullerene size beginning from C_{52}^- or C_{60}^- up to C_{136}^-, the largest investigated fullerene. A natural question then follows: Are these observations consistent across charged states, atomic and molecular systems and species as well?

We have addressed some of these issues recently [24] by studying the oxidation of water to peroxide using the doubly-charged standard reference C_{60}^{2-} anion, the negative metal ions Sn^{2-}, Pd^{2-}, Ag^{2-} and Au^{2-} and some lanthanide and actinide anions. The selection of the Sn^{2-}, Pd^{2-} and Au^{2-} anions has been motivated by the successful experiments [25 - 27] in catalyzing H_2O_2 formation from H_2 and O_2 using Au, Pd and Sn nanoparticles. Importantly, the experimenters [27] concluded that the inexpensive atomic Sn could be useful for water purification in the developing countries. Preliminary DFT TS calculations have found Pu^{2-}, Pa^{2-}, Sn^{2-} and La^{2-} the best catalysts among the investigated anions, including the C_{60}^{2-} anion in reducing the energy barrier considerably. Indeed, our finding that the Sn^{2-} anion reduces the TS energy barrier considerably is consistent with the experimental determination [27] and is reassuring. The negative ions of the highly radioactive Pu, Pa and At atoms should be ideal for catalyzing naturally a steady weak mixture of peroxide.

In the oxidation of water catalyzed by the oxygen-evolving complex of photosystem II the role of the Ca^{2+} was elucidated [1]. Previously, cationic systems were discovered to increase the TS energy barriers in the synthesis of peroxide from H_2O [28]. This could render them essential as inhibitors in controlling and regulating catalysis. Conversely, doubly-charged anionic systems may prove to be the effective optimal reaction promoters. These calculations provide further insight into the fundamental and comprehensive atomic theoretical framework for the next generation of tunable catalytic systems. The individual atoms and fullerenes explored here and in [23] could be used to systematically assemble various robust dynamic and tunable catalysts for differing functionality.

In the water oxidation to peroxide catalyzed by negative ions, two experiments provide an excellent understanding of the fundamental mechanism involved [29, 30]. Theoretically, deep insight is provided by the muon catalyzed nuclear fusion cycle involving the resonant formation of the muonic molecular ion, $dt\mu$ [20] and the interplay between Regge resonances and Ramsauer-Townsend minima in the electron elastic total cross sections (TCSs) along with the large EAs [31]. In the experiment [29], the vertical detachment energies (VDEs) of the Au^-M complexes (M = Ne, Ar, Kr, Xe, O_2, CH_4 and H_2O) were investigated. Importantly, the experiment discovered a stronger interaction between the Au^- anion and H_2O as well as between the Au^- and the CH_4 molecule. However, a weaker interaction was observed between the Au^- anion and O_2 as well as with the noble gases Ne, Ar, Kr, and Xe. Indeed, the anionic complexes $Au^-(H_2O)_2$ and $Au^-(H_2O)_1$ have been characterized as anionic Au^- interacting with two and one water molecules, respectively [30]. A similar analysis is applicable to the anionic molecular complex $Au^-(CH_4)$. The large EA of atomic Au played an essential role; it is important in the dissociation of the $Au^-(H_2O)_{2,1}$ anionic molecular complexes breaking up into the Au^- anion and $(H_2O)_{2,1}$[30]. Incidentally, these experiments [29,

30] probed the Au^- anionic catalysis at its fundamental level and demonstrate the importance of the EA in catalysis.

2. Results

2.1 Reaction dynamics

Following [31] in this study we first consider the slow oxidation process of water to peroxide without the negative-ion catalysts. We use the Au^- anionic catalyst to illustrate the mechanism in the reaction:

$$2H_2O + O_2 \rightarrow 2H_2O_2 \quad (1)$$

Then we apply the Au^- anion to speed up the reaction (1) and obtain

$$Au^-(H_2O)_2 + O_2 \rightarrow Au^- + 2\ H_2O_2. \quad (2)$$

$$Au^- + 4H_2O + O_2 \rightarrow Au^-(H_2O)_2 + 2\ H_2O_2. \quad (3)$$

Add reactions (2) and (3) and obtain

$$4H_2O + 2O_2 \rightarrow 4H_2O_2. \quad (4)$$

Similar results as in (4) are obtained when the Au^- anion is replaced by the various negative-ion catalysts considered here**.** The question we want to address here is which of the negative-ion catalysts speed up the reaction. Also, is a doubly-charged negative ion catalyst more effective in the catalysis of water to peroxide or vice versa? Very important here, the experiment [29] found a stronger interaction between the Au^- and H_2O and a weaker one between the Au^- and O_2. Indeed, the $Au^-(H_2O)_{1,2}$ anionic molecular complexes formation in the TS has been identified as the mechanism for breaking up the hydrogen bonding strength in water during catalysis.

2.2 Electron Scattering Total Cross Sections and Electron Affinity Calculations

For a better understanding and appreciation of the results presented here, namely doubly-charged negative ions as novel tunable mechanism for catalysis, we first present in Figs. 1-3 Regge-pole calculated low-energy electron scattering TCSs focusing on the large atoms such as the actinides. These are difficult to handle experimentally because of their radioactive nature. The interplay between Regge resonances and Ramsauer-Townsend (R-T) minima calculated through our Regge pole methodology has been identified as the fundamental atomic mechanism underlying nanoscale catalysis. Anionic catalysis involves the breaking up of the molecular bonds in the transition state (TS) [31]. The R-T minimum provides an excellent environment and mechanism for breaking up molecular bonds in new molecules creation as well as in anionic catalysis [31]. Generally, calculated low-energy electron elastic TCSs are characterized by dramatically sharp resonances manifesting ground, metastable and excited negative ion formation, with the ground state binding energies (BEs) yielding the important EAs that are theoretically challenging to calculate for complex heavy systems.

In Fig. 1 the standard elastic TCSs for the Au and C_{60} systems taken from [32], are displayed. They reveal the important characteristic negative ion BEs, R-T minima and shape resonances. It is noted here that the extracted anionic BEs from the ground state TCSs for Au and C_{60} are in outstanding agreement with the measured EAs for Au[30, 33, 34] and for C_{60} [35-37]. Figure 2 presents the Regge-pole calculated TCSs for the radioactive Th, Pa, U and Np actinide atoms. Except for the Th atom, no measurements of the EAs are available for any actinide atom. Very recently, the EAs of At was measured [21] as well as that of atomic Th [38]. However, the latter EA value has been identified with the BE of an excited state of Th [39]. Figure 3 compares the Regge-pole calculated TCSs for the large actinide atoms Cm and No. These

TCSs are also characterized generally by negative ion formation, shape resonances and R-T minima as well as exhibit atomic and fullerene molecular behavior near threshold [40]. Also, a polarization-induced metastable cross section with a deep R-T minimum near threshold is identified in the Cm TCSs. In the No TCSs this minimum has flipped over to a shape resonance appearing very close to threshold. We attribute these novel manifestations to size effects and orbital collapse impacting significantly the polarization interaction.

Importantly, the characteristic sharp peaks in the TCSs of these systems could be used to catalyze various reactions, including enzymes with VDEs within the BEs and R-T minima of the negative ion catalyst. Also, these results should help experiments and theory probe the long-overdue structure and dynamics of these poorly studied interesting actinide atoms.

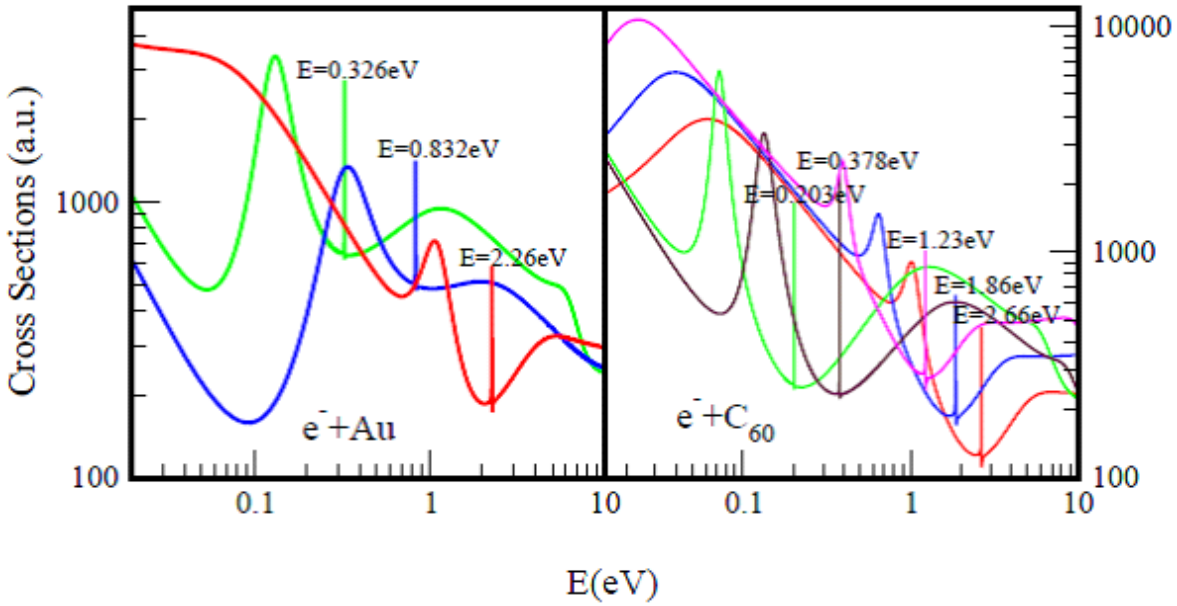

Figure 1: Standard total cross sections (TCSs) (a.u.) for electron elastic scattering from atomic Au (left panel) and the fullerene molecule C_{60} (right panel) are contrasted. For atomic Au the red, blue and green curves represent TCSs for the ground, metastable and excited states, respectively. For the C_{60} fullerene the red, blue and pink curves represent TCSs for the ground and the metastable states, respectively while the brown and green curves denote TCSs for the excited states. The dramatically sharp resonances in both figures correspond to the Au^- and C_{60}^- negative ions formation during the collisions.

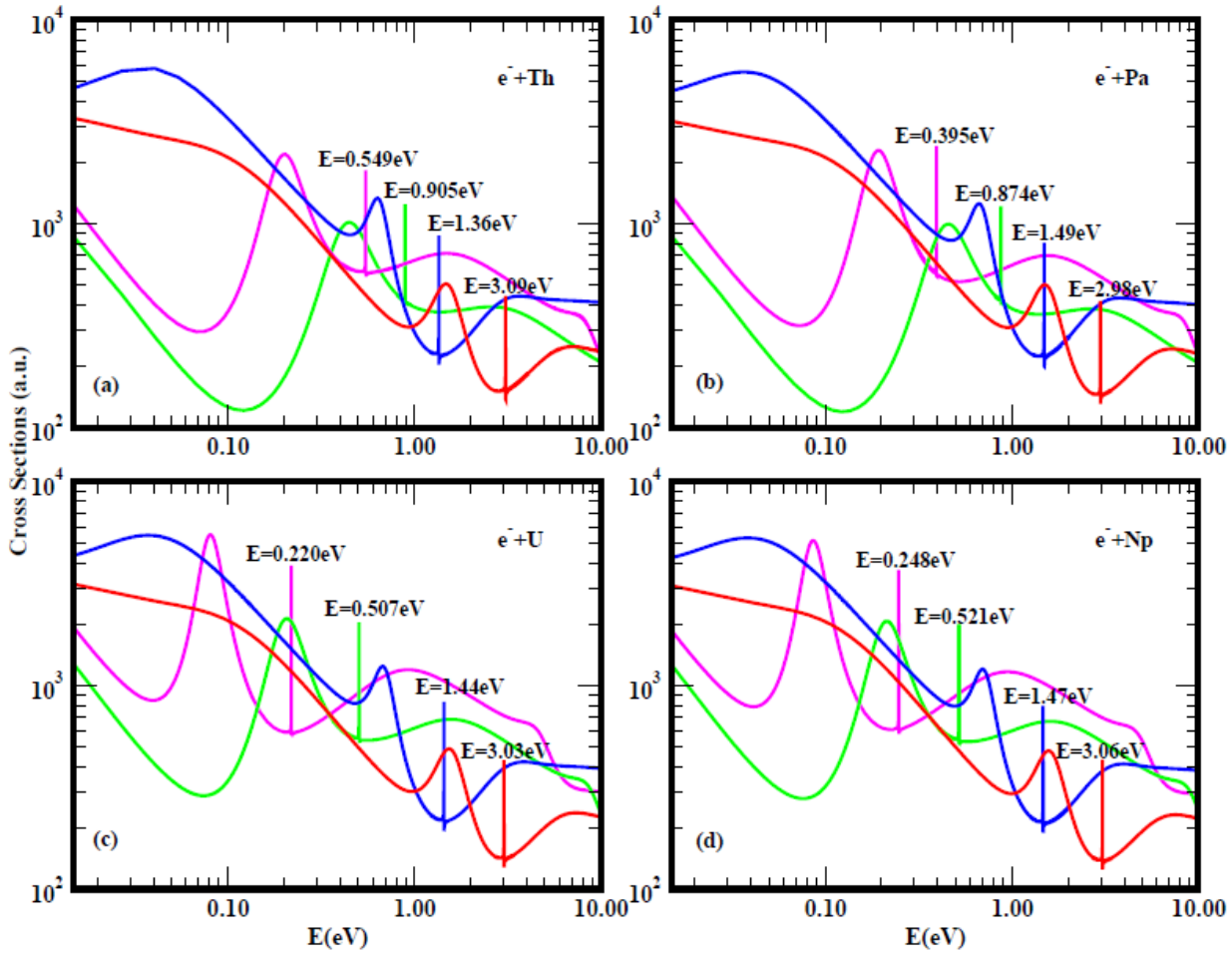

Figure 2: Total cross sections (a.u.) for electron elastic scattering from atomic Th(a), Pa(b), U(c) and Np(d). The red, blue, green and pink curves represent TCSs for the ground, metastable and two excited states, respectively. The dramatically sharp resonances in the figures correspond to the Th^-, Pa^-, U^- and Np^- negative ions formation during the collisions.

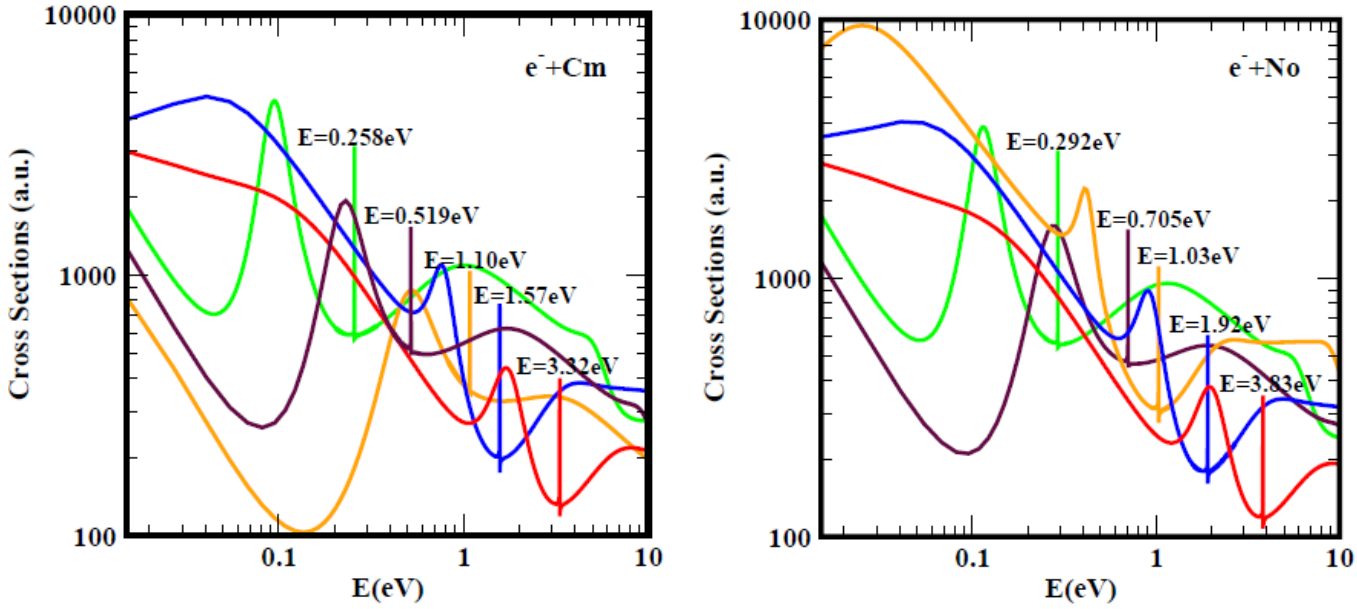

Figure 3: Total cross sections (a.u.) for electron elastic scattering from atomic Cm (left panel) and No (right panel) are contrasted. For both Cm and No the red, blue and orange curves represent TCSs for the ground and metastable states, respectively. The brown and green curves denote TCSs for the excited states. The dramatically sharp resonances in both figures correspond to the Cm^- and No^- negative ions formation during the collisions.

2.3 Transition State Energy Barriers Calculations

It has already been pointed out in the introduction that the fundamental mechanism underlying negative-ion catalysis involves anionic molecular complex formation in the TS with the atomic/molecular negative ion breaking up the bond-strength. Doubly-charged anionic transition state geometry optimized calculations of the Sn and Pu catalysts are shown in Figs 4 and 5, respectively. Figs 6 and 7 provide results for C60-6 and for graphene, Gr24-6, respectively. DFT and dispersion corrected DFT approaches have been employed for the transition state evaluations. The important communication conveyed by the figures here is the breakage of bonds in the transition state by the doubly-charged catalysts.

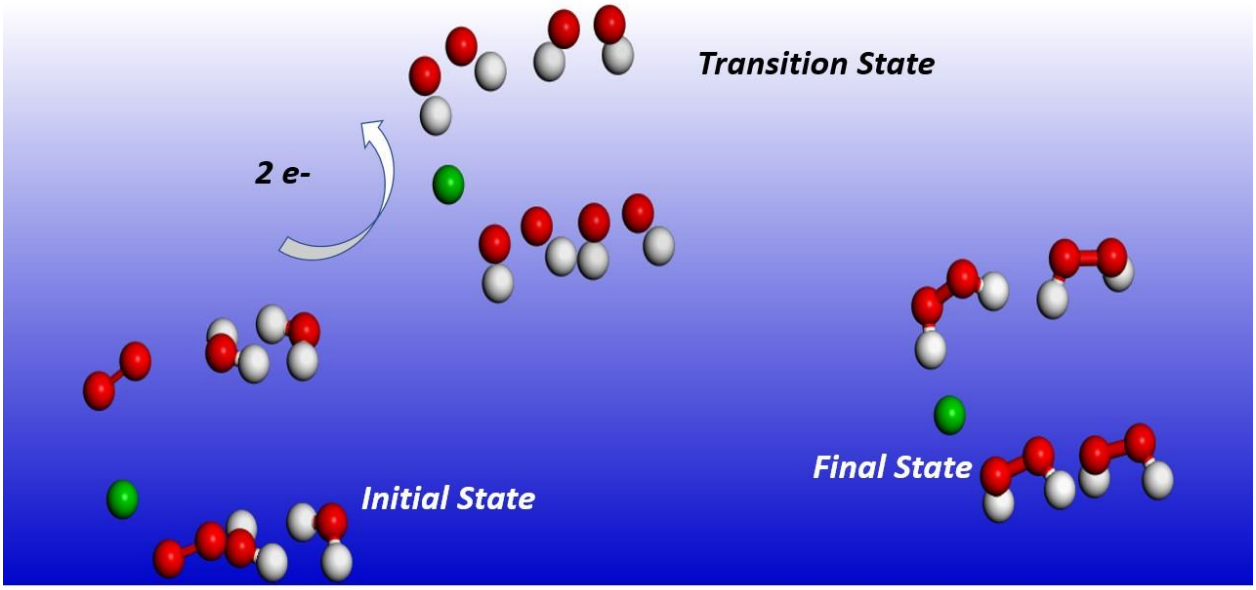

Figure 4: Doubly-charged anionic transition state geometry optimization for Sn. The red, white and green spheres represent O_2, H_2 and Sn (catalyst), respectively. Note the broken bonds in the transition state.

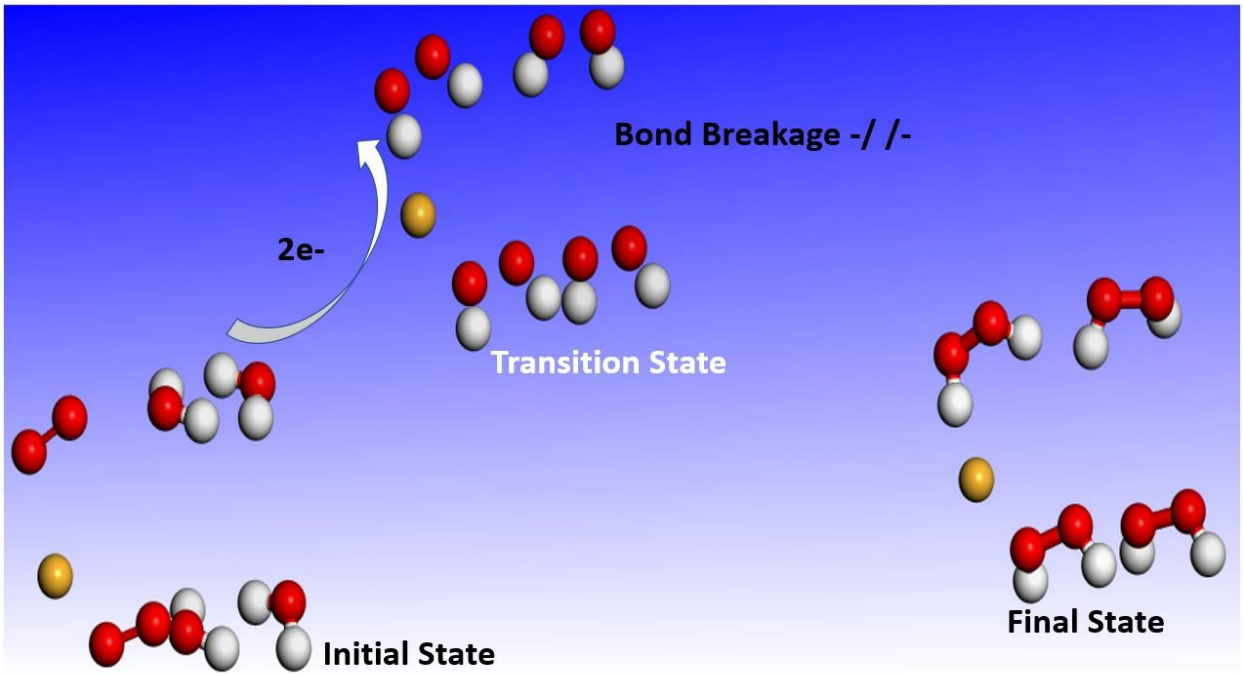

Figure 5: Doubly-charged anionic transition state geometry optimization for Pu. The red, white, and gold spheres represent O_2, H_2 and Pu (catalyst), respectively. Note the broken bonds in the transition state.

Preprints (www.preprints.org) | NOT PEER-REVIEWED | Posted: 6 August 2020 doi:10.20944/preprints202008.0142.v1

Peer-reviewed version available at Int. J. Mol. Sci. 2020, 21, 6714; doi:10.3390/ijms21186714

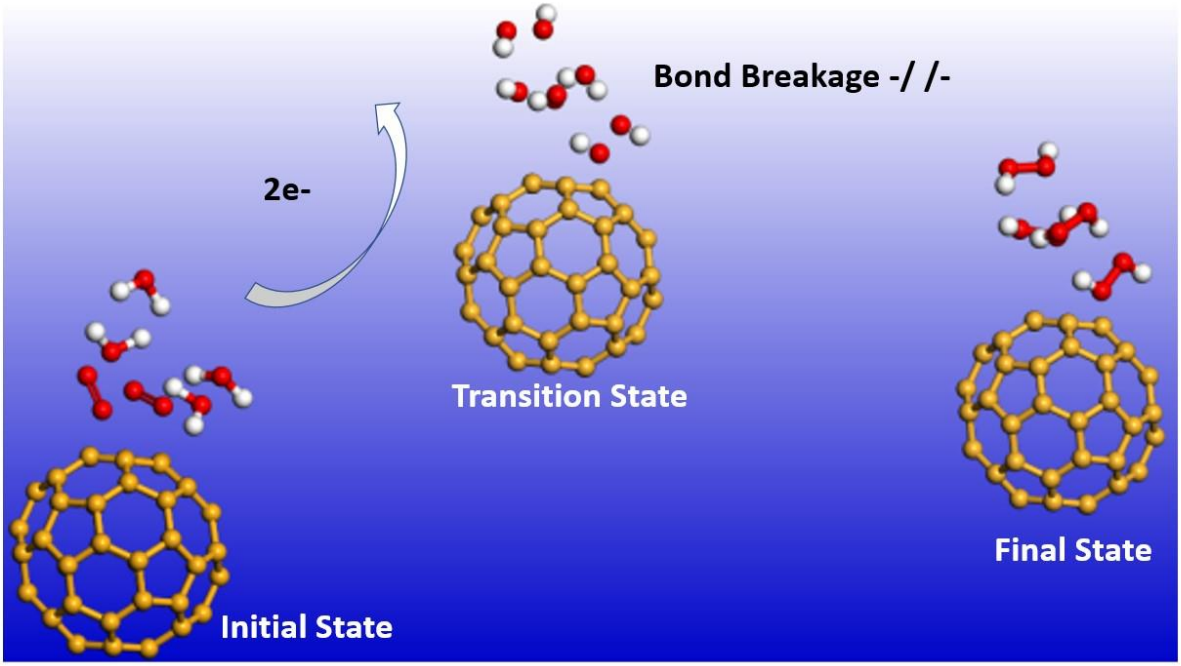

Figure 6: Doubly-charged anionic transition state optimization for C_{60}-6. The red, white and gold spheres represent O_2, H_2 and C_{60} (catalyst), respectively. Note that here also the bonds are broken in the transition state.

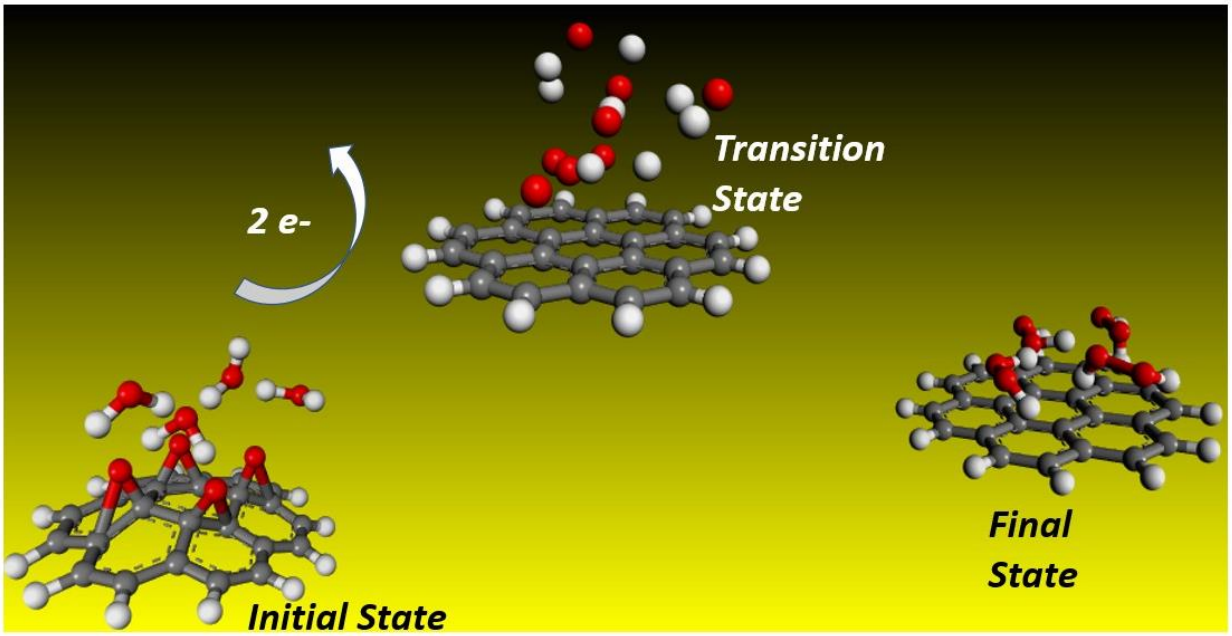

Figure 7: Geometrically optimized molecules of doubly-charged graphene Gr24-6 catalyzing water conversion to peroxide indicated by initial, transition, and final states. Carbon, Oxygen, and Hydrogen are

represented by the gray, red, and white spheres, respectively. Note here also that the bonds are broken in the transition state.

TABLE I: In Table 1 is presented the rank-ordered comparison of the activation energy barrier reduction by the doubly-charged systems, DCS(-2). These vary from the smallest investigated atom Si^{2-} with an energy value of 0.030eV to the largest atom U^{2-} with an energy value of 0.244eV. Also included in the Table I for comparison are the doubly-charged fullerene C_{20}, C_{60} and C_{136} as well as the graphene, Gr24-6 molecules. Indeed, the lowest energy reduction results from Si^{2-}. It is followed by the three radioactive elements Pu^{2-}, Pa^{2-} and At^{2-} with Sn^{2-} and La^{2-} close by with a value of about 0.1 eV. Clearly, the radioactive anions promise the realization of a dynamic tunable catalyst for the oxidation of water to peroxide without the need of an external power input. A visualization of the results is conveyed by the Figs. 8, 9 and 10. These Figs can also be used in selecting the appropriate doubly-charged systems for the oxidation of water to peroxide as well as in modeling more complex catalytic systems.

TABLE I: Rank-ordered activation energy barrier reduction, E(eV) for doubly-charged negative ionic systems, DCS(-2).

System S	DCS(-2) E(eV)	System S	DCS(-2) E(eV)	System S	DCS(-2) E(eV)
Si	0.030	Pt	0.283	Ti	1.074
Pu	0.087	Pd	0.297	V	1.100
Pa	0.092	Ni	0.342	Gr	1.130
-	-	Rh	0.403	C_{136}	1.440
At	0.098	Ag	0.429	C_{20}	2.070
Sn	0.103	O	0.443		
La	0.105	Co	0.541		
Zn	0.127	Au	0.575		
Eu	0.137	Ca	0.621		
Th	0.184	Cr	0.627		
U	0.244	Ce	0.710		
K	0.248	C_{60}	0.784		
Tm	0.273	Fe	0.879		
Cu	0.277	Mn	1.033		

Table II contrasts the activation energy barrier reduction by the doubly-charged systems, DCS(-2) with those by the singly-charged systems, SCS(-1). Generally, the DCS(-2) and SCS(-1) energies are close together for many of the systems considered here, implying that the SCS(-1) systems are already charge optimized. However, for Au and C_{136} the DCS(-2) energies are greater than those of the SCS(-1) by factors of about 1.44 and 2.11, respectively. This implies that decreasing the charge by -1 on the Au and C_{136} systems reduces their catalytic effectiveness, meaning that the energy barrier is increased by this change of charge. For Pa, Sn, Ca, and C_{60} the SCS(-1) values are greater than those of the DCS(-2) by factors of about 3.54, 11.75, 1.91 and 2.50, respectively. Indeed, the decrease of the charge by -1 in these systems increases their catalytic effectiveness by factors varying from 1.91 for Ca to 11.75 for Sn, allowing them to be charge-tunable.

The results in Table II demonstrate that in an environment where the charge on the systems could change, their catalytic effectiveness could increase or decrease. It is further noted that the catalytic effectiveness of C_{20} and graphene exhibit charge stability; namely, they remain unchanged when the charge changes from -

1 to -2 or vice versa. It can now be understood why the graphene molecule sometimes needs assistance from other atoms for effective catalysis.

TABLE II: Comparison of the activation energy barrier reduction, E(eV) between the doubly-charged systems, DCS(-2) and those by the singly-charged systems, SCS(-1).

System S	**E(eV) DCS(-2)**	**E(eV) SCS(-1)**			**System S**	**E(eV) DCS(-2)**	**E(eV) SCS(-1)**		
Si	0.030	-			Rh	0.403	0.420		
Pu	0.087	0.084			Ag	0.429	0.420		
Pa	0.092	0.326			Au	0.575	0.400		
At	0.098	0.172			Ca	0.621	1.188		
Sn	0.103	1.210			Cr	0.627	-		
La	0.105	0.035			C_{60}	0.784	1.960		
K	0.248	-			Gr	1.130	1.440		
Pt	0.283	0.323			C_{136}	1.440	0.680		
Pd	0.297	0.200			C_{20}	2.070	1.940		

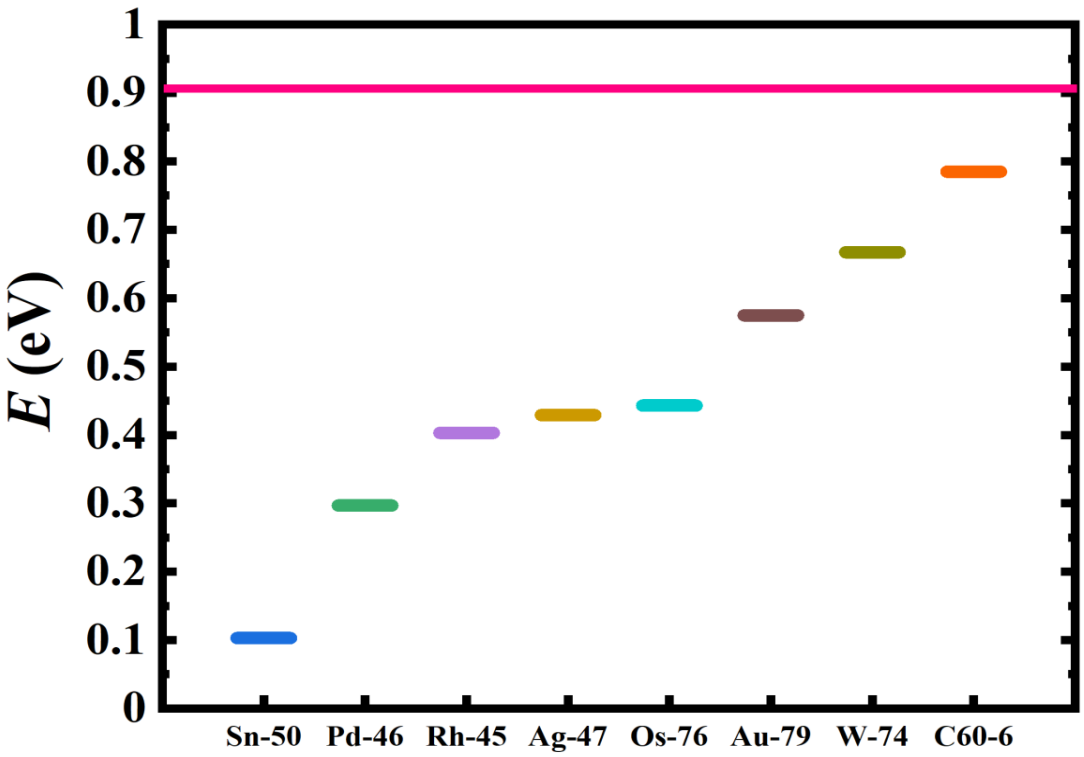

Figure 8: Transition state energy barrier reduction, E(eV) for selected doubly-charged anionic systems of popular catalysts in ascending order of catalytic effectiveness. The horizontal axis shows not to scale the catalyzing systems. The red line represents the energy position with no catalyst present.

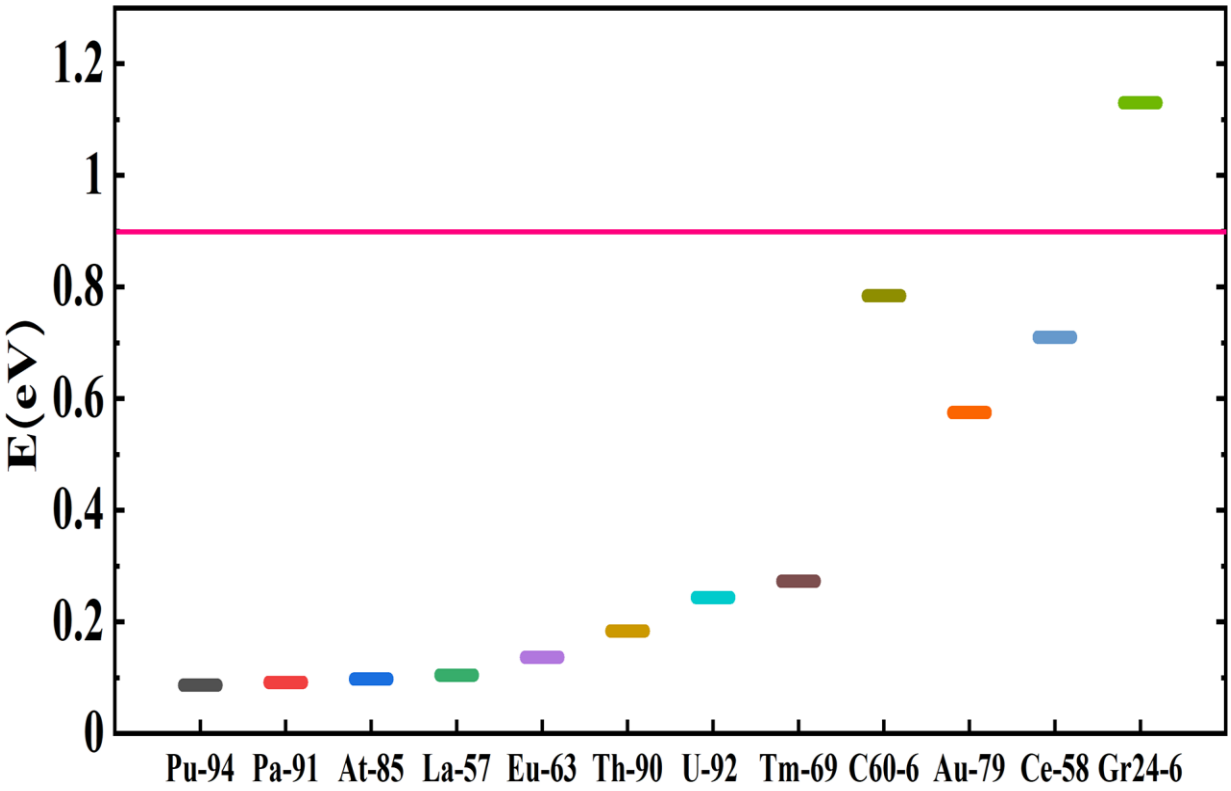

Figure 9: Transition state energy barrier reduction, E(eV) in ascending order of catalytic effectiveness for doubly-charged heavy systems, including C_{60} and 24 carbon graphene (Gr24-6). The horizontal axis not to scale indicates the catalyzing systems and the solid pink line represents the barrier energy position with no catalyst present.

Preprints (www.preprints.org) | NOT PEER-REVIEWED | Posted: 6 August 2020 doi:10.20944/preprints202008.0142.v1

Peer-reviewed version available at Int. J. Mol. Sci. 2020, 21, 6714; doi:10.3390/ijms21186714

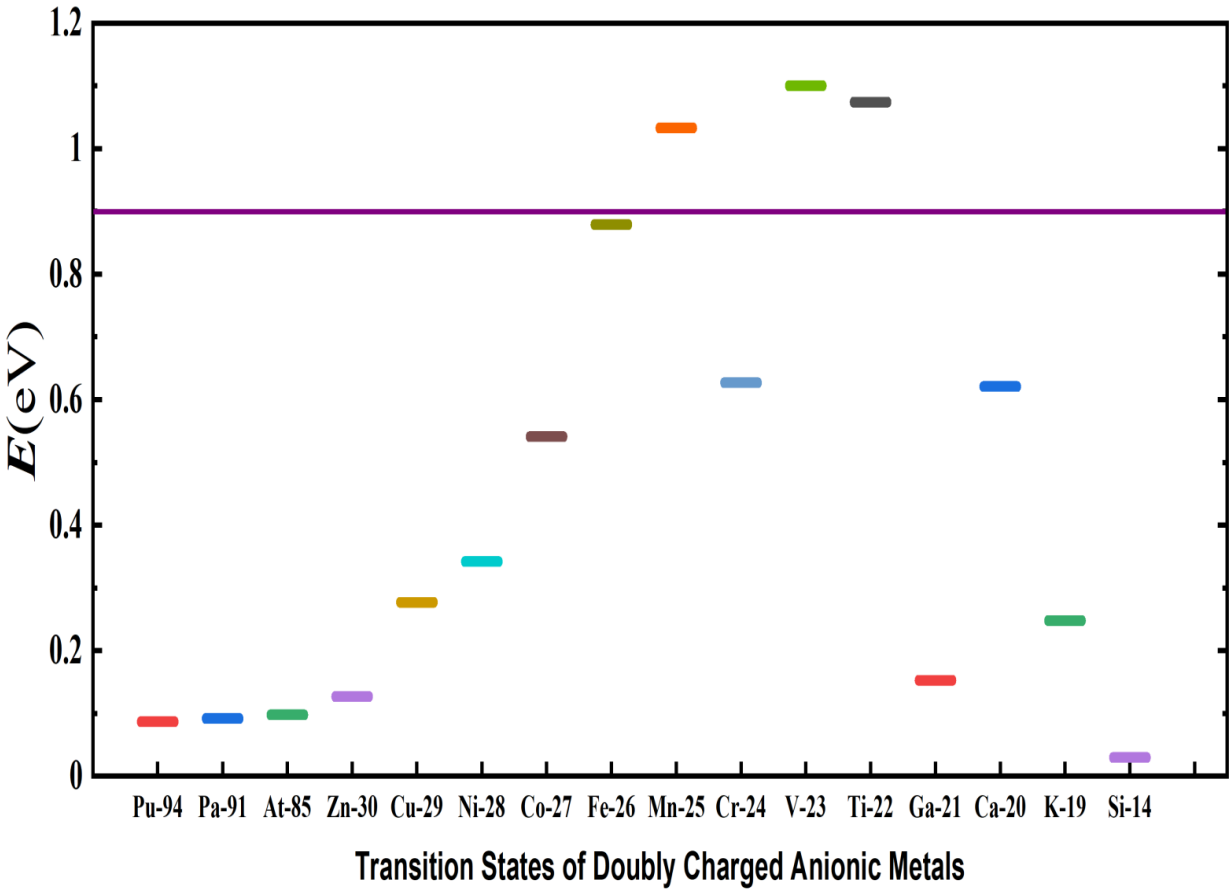

Figure 10: Transition state energy barrier reduction, E(eV) in ascending and descending order of catalytic effectiveness for doubly-charged atomic systems. The relative effectiveness of the popular components of catalysts from Z-30 to K-19 is emphasized. For high Z's the radioactive atoms are the most effective, while for the small ones, Si is the best doubly-charged catalyst. The horizontal axis reflects the catalyzing systems and the solid purple line shows the barrier energy position with no catalyst present.

3. Method of Calculation

3.1 Total Cross Sections Calculation

Regge poles, singularities of the S-matrix, rigorously define resonances [41, 42] and in the physical sheets of the complex plane they correspond to bound states [43]. Indeed, it has been confirmed that Regge poles formed during low-energy electron elastic scattering become stable bound states [44]. Being generalized bound states, they can be used to calculate reliably the BEs of the ground, metastable and excited states of the formed negative ions during the collision of an electron with complex heavy systems through the TCSs calculations. Here we adopt the Regge-pole methodology, also known as the complex angular momentum (CAM) method, for the calculation of the electron scattering TCSs. The near-threshold electron–atom/fullerene collision TCS resulting in negative ion formation is calculated using the Mulholland formula [45]. In the form below, the TCS fully embeds the essential electron-electron correlation effects [46, 47] (atomic units are used throughout):

$$\sigma_{tot}(E) = 4\pi k^{-2}\int_0^{\infty} \mathrm{Re}[1-S(\lambda)]\lambda d\lambda$$
$$-8\pi^2 k^{-2}\sum_n \mathrm{Im}\frac{\lambda_n \rho_n}{1+\exp(-2\pi i\lambda_n)} + I(E) \quad (5)$$

In Eq. (5) S(λ) and λ are respectively the S-matrix and the CAM, $k=\sqrt{2mE}$, m being the mass and E the impact energy, ρ_n is the residue of the S-matrix at the n^{th} pole, λ_n and $I(E)$ contains the contributions from the integrals along the imaginary λ-axis; its contribution has been demonstrated to be negligible [48].

As in [49] the complicated details of the electronic structure of the atom/fullerene itself are not considered here. The incident electron is assumed to interact with the complex atom/fullerene through the Thomas-Fermi type potential, known as the Avdonina, Belov and Felfli (ABF) potential [50] which accounts for the vital core-polarization interaction

$$U(r) = -\frac{Z}{r(1+\alpha Z^{1/3}r)(1+\beta Z^{2/3}r^2)} \quad (6)$$

In Eq. (6) Z is the nuclear charge, α and β are variation parameters. This potential has the appropriate asymptotic behavior, *viz.* $\sim -1/(\alpha\beta r^4)$ and accounts properly for the crucial polarization interaction at low energies. Extensively studied [51], the potential in Eq. (6) has five turning points and four poles connected by four cuts in the complex plane. The presence of the powers of Z as coefficients of r and r^2 in Eq. (6) ensures that spherical and non-spherical atoms/fullerenes as well as large and small systems are correctly treated. The effective potential $V(r)=U(r)+\lambda(\lambda+1)/2r^2$ is considered here as a continuous function of the variables r and complex λ. The details of the numerical evaluations of the TCSs have been described in [47] and further details of the calculations may be found in [52].

In the calculations, the optimal value of α was determined to be 0.2. When the TCS as a function of β has a dramatically sharp resonance [48], corresponding to the formation of a stable negative ion, this resonance is longest lived for a given value of the energy, which corresponds to the EA of the system (for ground state collisions) or the BE of the metastable/excited anion. Also calculated in the CAM methods are the important Regge Trajectories, viz. *Im* λ_n(E) versus *Re* λ_n(E). They have been used to demonstrate that at low energy relativistic and non-relativistic calculations yield essentially the same results [53].

3.2. Transition state energy barriers calculation

The utility of the formed doubly-charged negative ions has been demonstrated in the catalysis of water oxidation to peroxide using the various doubly-charged systems indicated under the results. Figures 4 - 6 demonstrate the Density Functional Theory (DFT) calculated transition states. DFT and dispersion corrected DFT approaches have been employed for the transition state evaluations. Geometry optimization of the structural molecular conformation utilized the gradient-corrected Perdew-Burke-Ernzerhof parameterizations [54] of exchange-correlation as implemented in DMol3 [55]. A tolerance of $1x10^{-3}$ Ha was used with a smearing value of 0.005 Ha. DFT calculated energy barriers reduction in the oxidation of H_2O to H_2O_2 catalyzed using the doubly-charged graphene, fullerene and atomic catalysts are shown in Figs. 4-10.

4. Concluding Remarks

We have investigated theoretically the catalytic effectiveness in the water oxidation to peroxide of various doubly-charged negative ions of atomic metals and contrasted their performance with that of the doubly-charged fullerene and graphene molecular anions. Density Functional Theory TS calculations have found tunable energy activation barrier reduction ranging from 0.030 eV to 2.070 eV, with Si^{2-}, Pu^{2-}, Pa^{2-} and Sn^{2-} as the best catalysts. This opens a new application opportunity for the radioactive actinide atoms. The C_{60}^{2-} reduces significantly the standard C_{60}^{-} transition state energy barrier while graphene increases it,

behaving more like cationic systems which previously were discovered to increase the TS energy barriers in the synthesis of peroxide from H_2O [56]. Our results should also be applicable to the petrochemical waste reduction of SO_2 by CO catalyzed by the nanosystem Au_5Cu^- [57] as well as in the conversion of methane to methanol without CO_2 emission. Rank-ordered doubly-charged negative-ion catalysts according to their energy barrier reduction, variation across charge states and systems are tabulated for easy selection for varied utility. They reveal their tunable nature and wide applications, ranging from water purification to biocompatible anti-viral and anti-bacterial sanitation systems. Indeed, the obtained here doubly-charged anionic catalysts offer a wide selection of atomic/molecular systems for the realization of inexpensive tunable dynamic water purification systems.

Acknowledgments: Research was supported by the U.S. DOE, Division of Chemical Sciences, Geosciences and Biosciences, Office of Basic Energy Sciences, Office of Energy Research, Grant: DE-FG02-97ER14743. The computing facilities of National Energy Research Scientific Computing Center, also funded by U.S. DOE are greatly appreciated. The authors thank Dr. Felfli for assisting with the calculation of the electron scattering cross sections.

Author Contributions: Conceptualization, methodology, investigation, formal analysis and writing of the original draft as well as rewriting and editing were carried out by both A.Z.M. and K.S. A.Z.M. is also responsible for securing the funding for the research.

Conflicts of Interest: The authors declare no conflict of interest or state.

References

1. Mauthe, S.; Fleischer, I.; Bernhardt, T.M.; Lang, S.M.; Barnett, R.N.; Landman, U. A Gas-Phase $Ca_n Mn_{4-n}O_4^+$ Cluster Model for the Oxygen-Evolving Complex of Photosystem II. *Angew Chem Int Ed Engl* **2019**, *58(25), 8504*. doi: 10.1002/anie.201903738.
2. Ruttinger, W.; Dismukes, G.C. Synthetic water-oxidation catalysts for artificial photosynthetic water oxidation. *Chem. Rev.* **1997**, 97, 1. doi.org/10.1021/cr950201z
3. Duan, L.; Bozoglian, F.; Mandal, S. *et al.* A molecular ruthenium catalyst with water-oxidation activity comparable to that of photosystem II. *Nature Chem.* **2012,** 4**,** 418. doi.org/10.1038/nchem.1301
4. Sartorel, A.; Carraro, M.; Scorrano, G.; Bonchio, M. Water Oxidation Catalysis by Molecular Metal-Oxides. *Energy Procedia* **2012**, 22, 78. doi.org/10.1016/j.egypro.2012.05.228Get
5. Du, P.; Eisenberg, R. Catalysts made of earth-abundant elements (Co, Ni, Fe) for water splitting: Recent progress and future challenges. *Energy & Environmental Science* **2012**, 5, 6012. DOI: 10.1039/C2EE03250C
6. Anantharaj, S.; Ede, S.R.; Sakthikumar, K.; Karthick, K.; Mishra, S.; Kundu, S. Recent Trends and Perspectives in Electrochemical Water Splitting with an Emphasis on Sulfide, Selenide, and Phosphide Catalysts of Fe, Co, and Ni: A Review. *ACS Catal.* 2016, 6, 12, 8069. doi.org/10.1021/acscatal.6b02479.
7. Jiao , Y.; Zheng, Y.; Jaroniec, M.; Qiao, S.Z. Design of Electrocatalysts for Oxygen- and Hydrogen-Involving Energy Conversion Reactions. *Chem. Soc. Rev.* **2015**, 44, 2060. DOI: 10.1039/c4cs00470a
8. Duan, J.; Chen, S.; Jaroniec, M.; Qiao, S.Z. Heteroatom-Doped Graphene-Based Materials for Energy-Relevant Electrocatalytic Processes. *ACS Catal.* 2015, 5, 9, 5207. doi.org/10.1021/acscatal.5b00991
9. Sayler, R.I.; Hunter, B.M.; Fu, W.; Gray, H.B.; Britt, R.D. EPR Spectroscopy of Iron- and Nickel-Doped [ZnAl]-Layered Double Hydroxides: Modeling Active Sites in Heterogeneous Water Oxidation Catalysts. *Journal of the American Chemical Society* **2020,** *142* (4), 1838. doi.org/10.1021/jacs.9b10273
10. Vogiatzis, K.D.; Polynski, M.V.; Kirkland, J.K.; Townsend, J.; Hashemi, A.; Liu, C.; Pidko, E.A. Computational Approach to Molecular Catalysis by 3d Transition Metals: Challenges and Opportunities. *Chemical Reviews* **2019,** *119* (4), 2453. doi.org/10.1021/acs.chemrev.8b00361

11. Mehrabani, S.; Bikas, R.; Zand, Z.; Suleyman I.; Mohammad, A.; Najafpour, M.. Water splitting by a pentanuclear iron complex. *Int. J. of Hydrogen Energy* 2020, 45, 17434. doi.org/10.1016/j.ijhydene.2020.04.249
12. Askerka, M.; Brudvig, G.W.; Batista, V.S. The O_2-Evolving Complex of Photosystem II: Recent Insights from Quantum Mechanics (QM/MM), Extended X-ray Absorption Fine Structure (EXAFS), and Femtosecond X-ray Crystallography Data. *Acc. Chem. Res.* **2017**, 50, 41. doi.org/10.1021/acs.accounts.6b00405
13. Liu, T.; Zhang, B.; Sun, L. Iron-Based Molecular Water Oxidation Catalysts: Abundant, Cheap, and Promising. Chemistry, An Asian J. **2018**. doi.org/10.1002/asia.201801253
14. Shylin, S.I.; Pavliuk, M.V.; D'Amario, L.; Mamedov, F.; Sá, J.; Berggren, G.; Fritsky, I.O. Efficient visible light-driven water oxidation catalysed by an iron(IV) clathrochelate complex. *Chem. Commun.* **2019**, 55, 3335. DOI: 10.1039/C9CC00229D
15. Yamamoto, K.; Takatsuka, K. Charge separation and successive reconfigurations of electronic and protonic states in a water-splitting catalytic cycle with the Mn4 CaO5 cluster. On the mechanism of water splitting in PSII. *Phys. Chem. Chem. Phys.* **2020,** *22, 7912.* DOI: 10.1039/D0CP00443J.
16. Zhang, Y.; Masuzaki, D.; Mafuné, F. Hydrophilicity and oxophilicity of the isolated CaMn4O5 cationic cluster modeling inorganic core of the oxygen-evolving complex. ***Chem. Commun.*** **2019**, ***55***, *14327*. DOI: 10.1039/C9CC07818E.
17. Moitra, P.; Alafeef, M.; Dighe, K.; Frieman, M.B.; Pan, D. Selective Naked-Eye Detection of SARS-CoV-2 Mediated by N Gene Targeted Antisense Oligonucleotide Capped Plasmonic Nanoparticles. *ACS Nano* 2020, *14, 6, 7617*. doi.org/10.1021/acsnano.0c03822
18. Iglesias-Mayor, A.; Amor-Gutiérrez, O.; Novelli, A.; Fernández-Sánchez, M-T,; Costa-García, A.; de la Escosura-Muñiz**,** A. Bifunctional Au@Pt/Au core@shell Nanoparticles As Novel Electrocatalytic Tags in Immunosensing: Application for Alzheimer's Disease Biomarker Detection. *Anal. Chem.* 2020, 92, 10, 7209. doi.org/10.1021/acs.analchem.0c00760
19. Speller, E.M. The significance of fullerene electron acceptors in organic solar cell photo-oxidation. *Materials Science and Technology* **2017**, 33:8, 924. DOI: 10.1080/02670836.2016.1215840
20. Armour, E.A.G. Muon, positron and antiproton interactions with atoms and molecules. *Journal of Physics: Conference Series* **2010**, 225, 012002. doi:10.1088/1742-6596/225/1/012002
21. Leimbach, D.; Sundberg, J.; Guo, Y.; Ahmed, R.; Ballof, J.; Bengtsson, L.; Pamies, F.B.; Borschevsky, A.; Chrysalidis, K.; Eliav, E.; *et al*. The electron affnity of astatine. arXiv **2002**, arXiv:2002.11418. **2020**
22. International Year of the Periodic Table: Single Atoms as Active Catalysts. Available online: https://pubs.rsc.org/en/journals/articlecollectionlanding?sercode=nr&themeid=1fc90a67-e081-4265-99eb-2201eb17c286 (accessed on 12 January **2017**).
23. Felfli, Z.; Suggs, K.; Nicholas, N.; Msezane, A.Z. Fullerene Negative Ions: Formation and Catalysis. *Int. J. Mol. Sci.* **2020**, *21*, 3159. doi.org/10.3390/ijms21093159
24. Msezane, A.Z.; Suggs, K. Doubly charged atomic negative ions for efficient tunable water oxidation to hydrogen peroxide. Open Access Government **2020**, July 27, pp 164-165 www.openaccessgovernment.org / www.pbctoday.co.uk
25. Edwards, J.K.; Carley, A.F.; Herzing, A.A.; Kiely, C.J.; Hutchings, G.J. Direct synthesis of hydrogen peroxide from H2 and O2 using supported Au–Pd catalysts. *J. Chem. Soc. Faraday Discuss* **2008**, *138*, 225. doi.org/10.1039/B705915A.
26. Edwards, J.K.; Solsona, B.; Landon, P.; Carley, A.F.; Herzing, A.; Watanabe, M.; Kiely, C.J.; Hutchings, G.J. Direct synthesis of hydrogen peroxide from H2 and O2 using Au–Pd/Fe2O3 catalysts. J. *Mater. Chem.* **2005**, *15*, 4595. doi: 10.1039/B509542E.
27. Freakley, S.J.; He, Q.; Harrhy, J.H.; Lu, L.; Crole, D.A.; Morgan, D.J.; E.N. Ntainjua, E.N.; Edwards, J.K.; Carley, A.F.; Borisevich, A.Y.; Kiely C.J.; Hutchings, G.J. Palladium-tin catalysts for the direct synthesis of H2O2 with high selectivity. *Science* **2016**, *351*, 959. doi: 10.1126/science.aad5705.

28. Tesfamichael, A.; Suggs, K.; Felfli, Z.; Wang, X. –Q.; Msezane, A. Z. Atomic gold and palladium negative ion-catalysis of water to peroxide: fundamental mechanism. *J. Nanoparticles Research* **2013**, 15, 1333
29. Gao, Y.; Huang, W.; Woodford, J.; Wang, L.–S.; Zeng, X. C. Detecting Weak Interactions between Au- and Gas Molecules: A Photoelectron Spectroscopic and Ab Initio Study. *J. Am. Chem. Soc*. **2009**, 131, 9484. DOI: 10.1021/ja903043d CCC
30. Zheng,W.; Li, X.; Eustis, S.; Grubisic, A.; Thomas, O.; De Clercq, H.; Bowen, K. Anion photoelectron spectroscopy of $Au^-(H2O)_{1,2}$, $Au_2^-(D2O)_{1-4}$, and $AuOH^-$. *Chem. Phys. Lett.* **2007**, 444, 232. doi:10.1016/j.cplett.2007.07.036.
31. Msezane, A. Z.; Felfli, Z.; Sokolovski, D. *J. Phys. B.* **2010**, 43, 201001. doi:10.1088/0953-4075/43/20/201001
32. Felfli, Z.; Msezane, A.Z. Negative Ion Formation in Low-Energy Electron Collisions with the Actinide Atoms Th, Pa, U, Np and Pu. *Applied Physics Research 2019, 11, 52. DOI: 10.5539/apr.v11n1p52*.
33. Hotop, H.; Lineberger, W.C. Dye-laser photodetachment studies of Au−, Pt−, PtN−, and Ag−. *J. Chem. Phys. 2003, 58, 2379, doi:10.1063/1.1679515.*
34. Andersen, T.; Haugen, H.K.; Hotop, H. Binding Energies in Atomic Negative Ions: III. *J. Phys. Chem. Ref. Data 1999, 28, 1511, doi:10.1063/1.556047*.
35. Huang, D.-L.; Dau, P.D.; Liu, H.T.; Wang, L.-S. High-resolution photoelectron imaging of cold C_{60}^- anions and accurate determination of the electron affinity of C_{60}. *J. Chem. Phys. 2014, 140, 224315. doi.org/10.1063/1.4881421*
36. Brink, C.; Andersen, L.H.; Hvelplund, P.; Mathur, D.; Voldstad, J.D. Laser photodetachment of C60− and C70− ions cooled in a storage ring. *Chem. Phys. Lett. 1995, 233, 52. doi.org/10.1016/0009-2614(94)01413-P*
37. Støchkel, K.; Andersen, J.U. Photo excitation and laser detachment of C60− anions in a storage ring. *J. Chem. Phys. 2013, 139, 164304. doi.org/10.1063/1.4826097*.
38. Tang, R.; Si, R.; Fei, Z.; Fu, X.; Lu, Y.; Brage, T.; Liu, H.; Chen, C.; Ning, C. Candidate for Laser Cooling of a Negative Ion: High-Resolution Photoelectron Imaging of Th−. *Phys. Rev. Lett. 2019, 123, 203002, doi:10.1103/PhysRevLett.123.203002.*
39. Felfli, Z.; Msezane, A.Z. Low-Energy Electron Elastic Total Cross Sections for Ho, Er, Tm, Yb, Lu, and Hf Atoms. *Atoms 2020, 8, 17; doi:10.3390/atoms8020017*
40. *Msezane, A.Z.; Felfli, Z. New insights in low-energy electron-fullerene interactions. Chem. Phys. 2018, 503, 50. doi.org/10.1016/j.chemphys.2018.02.005*
41. Frautschi, S.C. Regge Poles and S-matrix Theory (New York: Benjamin, 1963) Chapter X. doi.org/10.1063/1.
42. D'Alfaro, V.; Regge, T.E. Potential Scattering (Amsterdam: North-Holland, 1965)
43. Omnes, R.; Froissart, M. Mandelstam Theory and Regge Poles (New York: Benjamin, 1963) Chapt. 2
44. Hiscox, A.; Brown, B.M.; Marletta, M. On the low energy behavior of Regge poles. J. *Math. Phys.* **2010**, 51, *102104*. doi.org/10.1063/1.3496811
45. Mulholland, H.P. An asymptotic expansion for Σ(2n+1)exp (Àσ(n+1/2)2). *Proc. Camb. Phil. Soc.* (London) **1928**, *24*, 280–289, doi: 10.1017/S0305004100009074
46. Macek, J.H.; Krstic, P.S.; Ovchinnikov, S.Y. Regge Oscillations in Integral Cross Sections for Proton Impact on Atomic Hydrogen. *Phys. Rev. Lett.* **2004**, *93*, 183203. *doi.org/10.1103/PhysRevLett.93.183203*
47. Sokolovski, D.; Felfli, Z.; Ovchinnikov, S.Y.; Macek, J.H.; Msezane, A.Z. Regge oscillations in electron-atom elastic cross sections. *Phys. Rev. A* **2007**, *76*, 012705. DOI: 10.1103/PhysRevA.76.012705
48. Felfli, Z.; Msezane, A.Z.; Sokolovski, D. Resonances in low-energy electron elastic cross sections for lanthanide atoms. *Phys. Rev. A* **2009**, *79*, 012714. doi.org/10.1103/PhysRevA.79.012714

49. Dolmatov, V.K.; Amusia, M.Y.; Chernysheva, L.V. Electron elastic scattering off A@C60: The role of atomic polarization under confinement. Phys. Rev. A **2017**, 95, 012709. doi.org/10.1103/PhysRevA.95.012709
50. Felfli, Z.; Belov, S.; Avdonina, N.B.; Marletta, M.; Msezane, A.Z.; Naboko, S.N. in: J. Govaerts, M.N. Hounkonnou, A.Z. Msezane (Eds.), Proceedings of the Third International Workshop on Contemporary Problems in Mathematical Physics, World Scientific: Singapore, Singapore, 2004, pp. 218–232.
51. Belov, S.; Thylwe, K.-E.; Marletta, M.; Msezane, A.Z.; Naboko, S.N. On Regge pole trajectories for a rational function approximation of Thomas–Fermi potentials. *J. Phys. A* **2010**, *43*, 365301. doi.org/10.1088/1751-8113/43/36/365301
52. Burke, P.G.; Tate, C. A PROGRAM FOR CALCULATING REGGE TRAJECTORIES IN POTENTIAL SCATTERING. *Comp. Phys. Commun.* **1969**, *1*, 97. DOI: 10.1016/0010-4655(69)90003-4
53. Thylwe, K.W. On relativistic shifts of negative-ion resonances. *Eur. Phys. J. D* **2012**, *66*, 7 doi.org/10.1140/epjd/e2011-20530-4.
54. Tkatchenko, A.; Scheffler, M. Accurate Molecular Van Der Waals Interactions from Ground-State Electron Density and Free-Atom Reference Data. Phys. Rev. Lett. **2009**, *102*, 73005. doi.org/10.1103/PhysRevLett.102.073005.
55. DMol3 2011 Accelrys Software Inc.: San Diego, CA
56. Suggs, K.; Kiros, F.; Tesfamichael, A.; Felfli, Z.; Msezane, A.Z. Charge modification of metal atoms: Catalysis of Water to Peroxide. J. Phys: Conference Series **2015**, 635 052018. doi.org/10.1088/1742-6596/635/5/052018.
57. Hu, Y.-L.; Zhu, H.-R.; Wei, S.H. Single-doped charged gold cluster with highly selective catalytic activity for the reduction of SO2 by CO: First-principles study. *Chin. Phys. B.* 2019, 28(11), 113101. doi: 10.1088/1674-1056/ab4cdd